Examination of break-up fusion in the ^{16}O + ^{148}Nd system through measurements of forward recoil range distributions and angular distributions

Pankaj K. Giri ⬤,[1] Amritraj Mahato,[1] D. Singh,[1,*] Sneha B. Linda,[1] Harish Kumar,[2] Suhail A. Tali,[2] M. Afzal Ansari,[2]
R. Kumar,[3] S. Muralithar,[3] and R. P. Singh[3]

[1]*Department of Physics, Central University of Jharkhand, Ranchi 835 205, India*
[2]*Department of Physics, Aligarh Muslim University, Aligarh 202 002, India*
[3]*Inter University Accelerator Centre, Aruna Asaf Ali Marg, New Delhi 110 067, India*

The forward recoil range distributions and angular distributions of several evaporation residues produced via complete and incomplete fusion (ICF) dynamics in ^{16}O + ^{148}Nd system at energy $\approx$6 MeV/nucleon were measured. The measured forward recoil range distributions of various reaction products show the presence of incomplete fusion components apart from complete fusion. Full and partial linear momentum transfer components of reaction products were found in the interaction of ^{16}O with ^{148}Nd. These results were also confirmed by the measurements of angular distributions of evaporation residues. The measured angular distributions of the evaporation residues populated through complete and incomplete fusion channels were found to be distinctly different. The evaporation residues populated via complete fusion channels were trapped in the narrow angular zone as compared to incomplete fusion channels. A systematic study of the dependence of incomplete fusion dynamics on well-known entrance channel parameters shows that the incomplete fusion fraction grows exponentially with mass asymmetry (μ_{EC}^{AS}), Coulomb factor ($Z_P Z_T$) and α-Q value of the projectile. The present observations suggest an exponential rise of ICF fraction with entrance channel parameters in contrast with the linear pattern reported in some earlier measurements. Further, the correlation of incomplete fusion fraction with the structure of target (T) was investigated employing four different parameters viz. deformation parameter (β_2^T), interaction radius (R^T), deformation length ($\beta_2^T R^T$) and excess of neutrons $(N - Z)^T$ in the target. In the present study, the ICF fraction was found to rise exponentially with these parameters, independently for different projectiles. The three parameters β_2^T, $\beta_2^T R^T$, and $(N - Z)^T$ were found more sensitive and effective to investigate the entire picture about the influence of projectile and target deformation along with their relative orientations on incomplete fusion dynamics at low projectile energy. Moreover, the interaction radius of target (R^T) is suitable to explain the characteristics of ICF dynamics in the spherical-spherical collisions. These present results show that incomplete fusion dynamics is strongly affected by the structure of projectile along with the target.

I. INTRODUCTION

The study of the break-up of the projectile and incomplete fusion induced by heavy ions (HI) at low projectile energy has been a topic of special interest in nuclear physics [1–4]. It is a well-known fact that the complete fusion (CF) and incomplete fusion (ICF) are the most dominant modes of reaction in heavy-ion interactions at energy above the Coulomb barrier. As the incident projectile energy increases, the unambiguous reaction processes are the formation of the compound nucleus followed by the fusion of entire projectile with the target nucleus and decay of an excited compound nucleus. In this CF reaction, all nucleonic degrees of freedom are involved. However, for the projectile incident on target with relatively higher energy and impact parameter, the repulsive centrifugal potential increases. Hence, the dominance of attractive nuclear potential ceases to capture the entire projectile by the

target. Therefore, only a part of the projectile fuses with the target nucleus and the remnant behaves as a spectator, wherein an incompletely fused composite system may be formed and the ICF (break-up fusion) process may take place [5]. The probability of ICF reaction was experimentally observed for the first time [6] in the production of forward-peaked fast α particles in the break-up of the projectiles ^{16}O, ^{14}N, and ^{12}C at energy $\approx$10.5 MeV/nucleon. However, the advances in the study of ICF dynamics took place after the measurements of transition intensity distributions (spin distribution) of evaporation residues (ERs) using particle γ-coincidence technique [7]. Evidence for the ICF process was also found by measuring the forward-peaked α particles in the kinetic energy spectra and angular distribution of α particles [8] and from time-of-flight measurements [9] of ERs. The analysis of measured excitation functions (EFs) data [10–12] shows that the ICF process has a substantial contribution to the reaction cross sections.

Several theoretical models were proposed to explain the ICF dynamics, such as break-up fusion (BUF) model [13],

*Corresponding author: dsinghcuj@gmail.com

sumrule model [14], promptly emitted particles (PEP) model [15], hot spot model [16], and Fermi-jet model [17], etc. As a matter of fact all these models have been used to fit the experimental data of projectile like fragments (PLFs) at projectile energy above 10 MeV/nucleon. However, no theoretical model exists in the literature to reproduce the gross feature of ICF experimental data at low projectile energy. As such, the study of ICF dynamics is an area of keen interest for investigation.

In recent years, major interest has been shown by investigators to study the dependence of ICF dynamics on various entrance channel parameters (e.g., mass asymmetry, α-Q value, $Z_P Z_T$, etc.) [18–21]. These studies show that a single entrance channel parameter does not explain entirely the incomplete fusion contribution at low energy. Some measurements [22,23] show distinctly different spin distributions and feeding intensity patterns of ERs populated through CF and ICF. Recent studies [24] highlight the role of target deformation on ICF dynamics at projectile energy above the fusion barrier (F_{br}).

Various experimental techniques have been employed for the study of ICF dynamics such as excitation functions (EFs) measurements, kinetic energy spectra, and angular distribution of projectile like fragments (PLFs), forward recoil range distributions (FRRDs), spin distributions and feeding intensity pattern using particle γ-ray coincidence of ERs.

The onset of dependence of ICF dynamics on various entrance channel parameters is still ambiguous and needs special attention. To investigate ICF reaction dynamics in detail, a series of experiments was performed employing different techniques. The ICF fractions were deduced from those measured data and compared with literature data in terms of various entrance channel parameters. In this respect, recent work [25] reported by our group shows the dependence of ICF dynamics on the target deformation through the measurements of excitation functions of evaporation residues populated via CF and/or ICF dynamics in the interaction of ^{16}O with ^{148}Nd target at projectile energy $\approx$4–7 MeV/nucleon. As an extension of previous work [25], to have a better understanding of fusion incompleteness, two experimental techniques viz. (i) the forward recoil range distributions (FRRDs) and (ii) angular distributions (ADs) for the ERs populated through CF and/or ICF in the same system at projectile energy $\approx$6 MeV/nucleon were further employed. The results reported [25] by excitation functions measurements of CF and ICF residues have also been further confirmed by the FRRDs measurements for same system and energy. The relative contributions of CF and ICF products were separated out from the present data of FRRDs. The ICF fraction (F_{ICF}) for the present measurements was compared with some other systems available in the literature. The literature survey shows that very limited study using ADs of ERs populated through CF and ICF dynamics is available. As such, the present results of FRRDs measurement were also supported by ADs measurements for above-mentioned system at same energy. On the other hand, a systematic study for dependence of ICF dynamics on the deformation of target (T) was also done employing deformation parameter (β_2^T), interaction radius (R^T), deformation length ($\beta_2^T R^T$), and neutron excess ($N - Z)^T$.

The present paper is organized as follows: the experimental techniques are given in Sec. II. Interpretation of the experimental results are discussed in Sec. III. The discussion of ICF fraction and its correlation with entrance channel effects is given in Sec. IV. The summary and conclusion of the present study are given in Sec. V.

II. EXPERIMENTAL TECHNIQUES EMPLOYED FOR THE MEASUREMENTS OF FRRDs AND ADs

The present experiments were performed using 15 UD Pelletron at Inter University Accelerator Centre (IUAC), New Delhi, India. Measurements of forward recoil range distributions (FRRDs) and angular distributions (ADs) of ERs were carried out in the general purpose scattering chamber (GPSC). This scattering chamber has an in-vacuum transfer facility (IVTF) to minimize the time lapse between the end of irradiation and the start of counting of the samples. The stacked foil activation technique followed by off-line γ ray spectrometry was employed to determine the measured yields for various ERs. The targets of ^{148}Nd (enrichment $\approx$98.4%) used in these measurements (FRRDs and ADs) were prepared by vacuum evaporation technique in target fabrication laboratory at IUAC, New Delhi. In the FRRDs experiment, nineteen thin ^{27}Al catcher foils of thickness $\approx$40–60 μg/cm^2 were used to trap the recoiling ERs. These thin aluminium (^{27}Al) catcher foils were prepared by vacuum evaporation technique. The thickness of targets and ^{27}Al catcher foils was determined using the α-particle transmission method as well as Rutherford back scattering (RBS) technique [26]. The thickness of ^{27}Al catcher foils were determined using the α-particle transmission method. The α-particle transmission method is based on the energy loss of 5.485 MeV α particles emitted from a ^{241}Am source in target and aluminium catcher foils. Energy dispersive x-ray spectroscopy (EDXS) [27] technique was employed to check the purity of targets. The target and ^{27}Al catchers were pasted on rectangular ^{27}Al holders having concentric holes of 1.0 cm diameter. The effective projectile energy on the target has been estimated by calculating energy loss in the middle of the ^{148}Nd target. The irradiation of this stack was done using ^{16}O^{7+} beam at projectile energy $\approx$6 MeV/nucleon. The stack was irradiated for about 11 h due to the half-lives of ERs of interest. The beam current during the irradiation of stack was maintained $\approx$2–3 pnA. The flux of ^{16}O ion beam was determined using a Faraday cup placed at the end of the scattering chamber behind the target-catcher foil arrangement.

Further, the angular distributions (ADs) of ERs produced in the system ^{16}O + ^{148}Nd have also been measured at energy $\approx$6 MeV/nucleon. The ^{148}Nd target of thickness $\approx$0.30 mg/cm^2 supported by Al backing was used for ADs measurements. A stack of thick annular concentric Al catcher rings of thickness $\approx$0.5 mm was employed to trap the ERs. The angular stack was consisting of thick concentric annular Al catchers of diameters 0.5 cm, 0.8 cm, 1.3 cm, 1.8 cm, 2.3 cm, 3.0 cm, and 4.0 cm, respectively. These Al rings correspond to seven forward angular zones, viz., 0°–8°, 8°–12°, 12°–20°, 20°–27°, 27°–34°, 34°–42°, and 42°–51°. This arrangement of angular rings was placed 1.7 cm behind
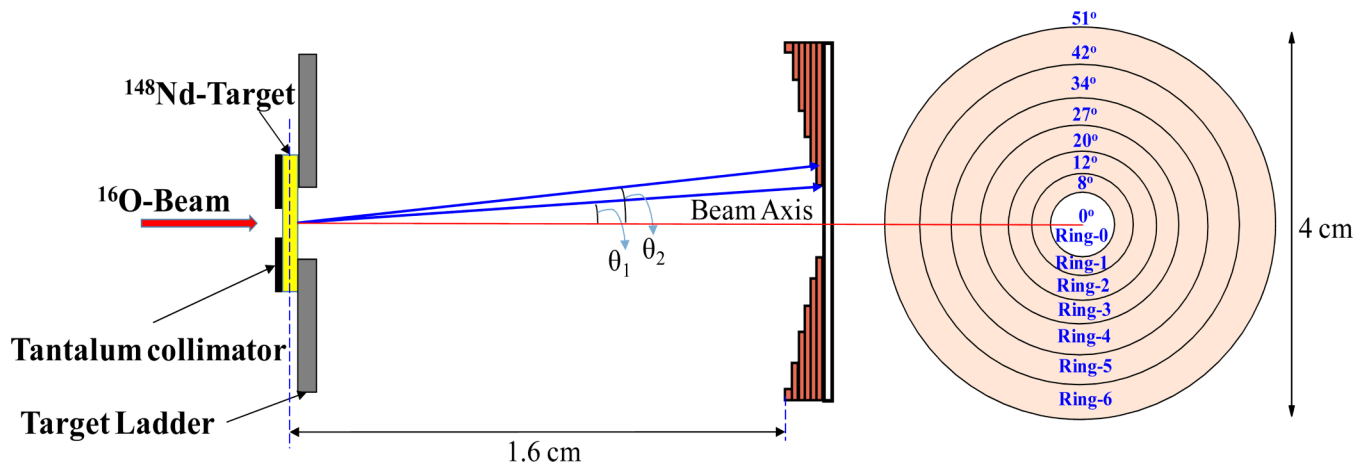
FIG. 1. Experimental setup used for the measurement of angular distributions (ADs) of ERs populated via CF and/or ICF in the ^{16}O + ^{148}Nd system at projectile energy ≈ 6 MeV/nucleon.

the target for collecting the ERs populated in the irradiation of target. The target irradiation was carried out for ≈ 9 h. The average beam current during the irradiation was monitored ≈ 2–3 pnA. A typical annular stack of target-catcher assembly covering the angular zone $0°$–$8°$ to $42°$–$51°$ employed for the measurement of ADs of ERs is displayed in Fig. 1.

After the irradiation, the stacks of ^{27}Al catchers along with ^{148}Nd targets were taken out from the scattering chamber using IVTF. The target-catcher assembly was dismantled to record the activities induced in the individual irradiated catcher foil. The activities induced in each ^{27}Al catcher was recorded individually at increasing time intervals using a precalibrated high-resolution high-purity germanium (HPGe) γ-ray spectrometer coupled to a CAMAC-based personal computer employing CANDLE software [28]. The HPGe γ-ray spectrometer (resolution 2 keV for 1.408 MeV γ ray of ^{152}Eu) was calibrated for energy and efficiency. To determine the geometry-dependent efficiency of the HPGe detector at various source-detector distances, a standard source of ^{152}Eu of known strength was used. The induced activity in various ^{27}Al catchers were used to measure the production probability of different ERs. The identification of ERs was done on the basis of their characteristic γ rays and also by following their half-lives. Typical γ spectra recorded for the FRRDs (cumulative thickness ≈ 676 μg/cm^2) and ADs (angular zone $0°$–$8°$) showing some of the identified γ peaks at energy $\approx$ 6 MeV/nucleon are shown in Figs. 2–3. The spectroscopic data used in the determination of production cross sections of various ERs were taken from Refs. [29–31]. A list of identified ERs produced via CF and/or ICF dynamics in ^{16}O + ^{148}Nd system along with their decay characteristics is given in Table I. The measured cross sections $\sigma_{ER}(E)$ for a particular ER were calculated using the standard formulation given in Ref. [32].

The measured yields of an ER as a function of the range in stopping medium are associated with errors and uncertainties in the thickness of target and catcher foils, counting statistics, etc. The overall errors in the measured production yield from various factors were estimated to be less than 15%. More

details of the various factors responsible for the errors and uncertainties in the measured data is given in Ref. [25].

III. ANALYSIS OF EXPERIMENTAL RESULTS

In the present work, the analysis of FRRDs for different ERs was performed within the framework of the degree of linear momentum transfer from the projectile to the target nucleus by adopting break-up fusion model considerations. In the case of ADs measurements, the analysis of the present results was done by using statistical model code PACE4. The detailed analysis of both FRRDs and ADs measurements are presented in the following sections.

A. Forward recoil range distributions (FRRDs) of ERs

The FRRDs for the ERs ^{159,158}Er(xn), ^{160g,159}Ho(pxn), ^{157,155}Dy(αxn), and ^{155}Tb($\alpha\,pxn$) produced in the collision of ^{16}O with ^{148}Nd at projectile energy ≈ 6 MeV/nucleon were measured. In FRRDs measurements, the measured cross section of the ERs in each catcher foil was divided by its thickness to obtain the normalized yield of ER. These normalized yields of different ERs were plotted as function of cumulative catcher thickness to obtain differential recoil
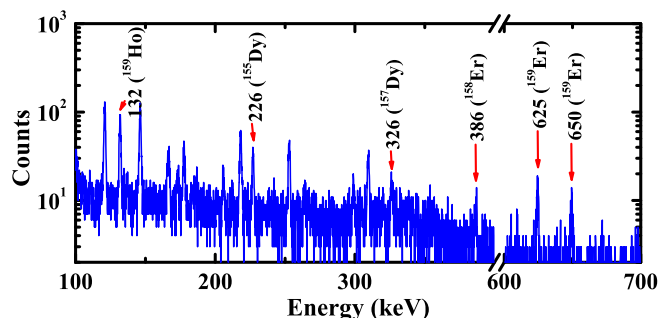

FIG. 2. Typical γ ray spectrum of induced activity in the Al catchers recorded in the measurement of FRRDs at cumulative thickness ≈ 676 μg/cm^2 after the interaction of projectile ^{16}O with ^{148}Nd at energy ≈ 6 MeV/nucleon.
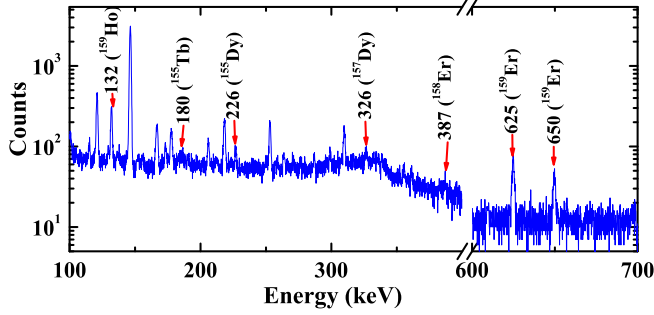
FIG. 3. Typical γ-ray spectrum of induced activity in the Al catcher recorded in the measurement of ADs covering the annular zone $0°$–$8°$ for the $^{16}O + {}^{148}Nd$ system at projectile energy ≈ 6 MeV/nucleon.

range distributions of the identified ERs. The measurement of FRRDs may provide significant information on the degree of linear momentum transfer from the projectile to target and may give the involved reaction mechanism. The relative contributions of various ERs produced via CF and/or ICF processes were computed by fitting the measured FRRDs data with Gaussian composite peaks using the ORIGIN software [33], similar to that given in Ref. [34].

The theoretical forward recoil ranges of ERs were also computed using the code stopping power and range of ions in materials (SRIM-2008) [35]. The measured most probable ranges (R^{MP}_{Expt}) for the identified ERs deduced from FRRDs plots along with the theoretical mean ranges (R^{MP}_{Theo}) are given in Table II. The theoretical mean forward recoil ranges have been calculated assuming the break-up fusion model, i.e., (i) for CF, ^{16}O projectile completely fuses with ^{148}Nd target and entire linear momentum is transferred to the compound nucleus and (ii) for ICF, ^{16}O projectile breaks up into fragments $^{12}C + \alpha$. In this process, the fragment ^{12}C fuses with ^{148}Nd nucleus and α particle fly in the forward direction with almost same velocity of the projectile. The measured forward recoil range distributions of ERs produced via CF and ICF are displayed in Figs. 4–5. The measured data are shown by solid spheres and the fitted data are shown by
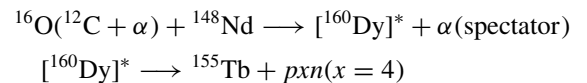
TABLE I. List of identified ERs populated via CF and ICF channels along with half-lives, identified γ rays and branching ratios in $^{16}O + {}^{148}Nd$ system at projectile energy ≈ 6 MeV/nucleon. (g: ground state; min: minutes; h: hours; d: days.)

S. No.	Evaporation Residue	Half-life ($T_{1/2}$)	E_γ (keV)	$\theta\%$
1.	$^{159}Er(5n)$	36.00 min	625	33.00
			650	23.40
2.	$^{158}Er(6n)$	2.29 h	387	9.00
			248	3.42
3.	$^{160}Ho(p3n)$	25.60 min (g)	728	14.60
4.	$^{159}Ho(p4n)$	33.00 min	132	23.60
5.	$^{157}Dy(\alpha 3n)$	8.10 h	326	92.00
6.	$^{155}Dy(\alpha 5n)$	10.00 h	226	68.40
7.	$^{155}Tb(\alpha p4n)$	5.32 d	180	7.45
			262	5.30

shaded area of the plots. In Figs. 4(a)–4(d), the FRRDs of ERs $^{159}Er(5n)$, $^{158}Er(6n)$, $^{160g}Ho(p3n)$, ^{159}Ho ($p4n$) show a single peak corresponding to the cumulative thicknesses $\approx 615 \pm 23$, $\approx 604 \pm 25$, $\approx 590 \pm 26$, and $\approx 601 \pm 23\,\mu g/cm^2$, respectively. The measured most probable ranges for these ERs are found to be in good agreement with theoretically calculated mean range $\approx 611\,\mu g/cm^2$, which clearly shows that these ERs are formed via only CF of ^{16}O with ^{148}Nd. Therefore the relative contribution of CF for the ERs $^{159}Er(5n)$, $^{158}Er(6n)$, $^{160g}Ho(p3n)$, and $^{159}Ho(p4n)$ are found to be $\approx 100\%$. Further, it can be observed from Figs. 5(a)–5(c), the FRRDs of ERs ^{157}Dy and, ^{155}Dy may be fitted with two Gaussian peaks, one at larger cumulative catcher thickness $605 \pm 48\,\mu g/cm^2$ and, $644 \pm 50\,\mu g/cm^2$, respectively, while another peak at smaller cumulative thickness $405 \pm 22\,\mu g/cm^2$ and, $384 \pm 19\,\mu g/cm^2$, respectively. The peak at larger cumulative thickness indicates the complete momentum transfer component. Hence, the peak corresponding to larger cumulative thickness for the ERs ^{157}Dy and ^{155}Dy is attributed to the population of these ERs via CF process. On the other hand, the peak observed at smaller cumulative catcher thickness is produced due to the incomplete fusion of ^{16}O (fusion of fragment ^{12}C), because the partial linear momentum transferred is expected to be less than that for the CF of ^{16}O with the target ^{148}Nd. This indicates that the ERs ^{157}Dy and ^{155}Dy may have contribution not only from CF of ^{16}O but also have a contribution from ICF of ^{16}O (fusion of ^{12}C with ^{148}Nd).

The observed forward recoil ranges of these ERs agree well with the theoretical mean recoil ranges of the compound system $^{164}Er^*$ and composite system $^{160}Dy^*$ in the stopping medium. The relative contributions of the ICF for ERs ^{157}Dy and ^{155}Dy were found to be $\approx 77\%$, and $\approx 35\%$, respectively, while for these ERs, CF contributions were $\approx 23\%$, and $\approx 65\%$ respectively as shown in Figs. 5(a)–5(b).

The FRRDs of ER ^{155}Tb ($\alpha p4n$) as shown in Fig. 5(c), shows only a single peak at a cumulative thickness $\approx 372 \pm 16\,\mu g/cm^2$. The experimental forward recoil range (R^{MP}_{Expt}) for ^{155}Tb agrees well with the theoretical most probable range (R^{MP}_{Theo}) calculated for the composite system $^{160}Dy^*$ (fusion of ^{12}C with ^{148}Nd) in the stopping medium. There is no complete fusion peak observed in the FRRDs analysis for this ER. This indicates that the ER ^{155}Tb may be populated solely via ICF of ^{16}O with ^{148}Nd. In this process, partial linear momentum transfer from projectile to the composite system may take place. In the case of this ER, the relative contribution of incomplete fusion (ICF) was found to be $\approx 100\%$ as shown in Fig. 5(c). As a representative case, the ER ^{155}Tb is likely to be populated via the following reaction route;

$$^{16}O(^{12}C + \alpha) + {}^{148}Nd \longrightarrow [^{160}Dy]^* + \alpha(\text{spectator})$$
$$[^{160}Dy]^* \longrightarrow {}^{155}Tb + pxn(x = 4)$$

The comparison of measured and theoretically predicted results may provide a key to understand the involved reaction mechanism in the production of evaporation residues. The right choice of the parameters used after the optimization in theoretical predictions through the statistical model code is a requisite step for the analysis. In the present work, the statistical model calculations have been done using two codes

TABLE II. Experimentally measured most probable ranges (R_{Expt}^{MP}) deduced from FRRD curves and theoretically calculated mean ranges (R_{Theo}^{MP}) for CF and ICF components produced in the interaction of ^{16}O with ^{148}Nd at ≈ 6 MeV/nucleon energy.

S. No.	Evaporation Residue	CF of ^{16}O beam with ^{148}Nd		ICF of ^{16}O beam (^{12}C fusion with ^{148}Nd)	
		$^{CF}R_{\text{Theo}}^{MP}$ (μg/cm^2)	$^{CF}R_{\text{Expt}}^{MP}$ (μg/cm^2)	$^{ICF}R_{\text{Theo}}^{MP}$ (μg/cm^2)	$^{ICF}R_{\text{Expt}}^{MP}$ (μg/cm^2)
1.	^{159}Er(5n)	611	615 ± 23	381	–
2.	^{158}Er(6n)	611	604 ± 25	381	–
3.	^{160g}Ho(p3n)	611	590 ± 26	381	–
4.	^{159}Ho(p4n)	611	601 ± 23	381	–
5.	^{157}Dy(α 3n)	611	605 ± 48	381	405 ± 22
6.	^{155}Dy(α 5n)	611	644 ± 50	381	384 ± 19
7.	^{155}Tb(α p4n)	611	–	381	372 ± 16

PACE4 [36–38] and CASCADE [39] to compare the range integrated yields of ERs $\sigma_{\text{Expt}}^{FRRD}$ populated via CF and ICF channels. The codes PACE4 and CASCADE are based on the Hauser-Feshbach formalism of CN decay [40]. These codes take into account the statistically equilibrated emission of light particles (i.e., neutron, proton, and α particle, etc.) and γ rays, only for the decay of the compound nucleus. The possibility of ICF, and/or preequilibrium (PE) emission are not considered in both codes. In these codes, level density parameter $a(= A/K)$ MeV^{-1} is an important parameter, where A is the mass number of the CN and K is the level density parameter constant. In the present work for the ^{16}O + ^{148}Nd system, $K = 10$ has been taken in the PACE4 and CASCADE calculations. More details about the analysis of data using PACE4 code is given in our previous work [25] for the same system.
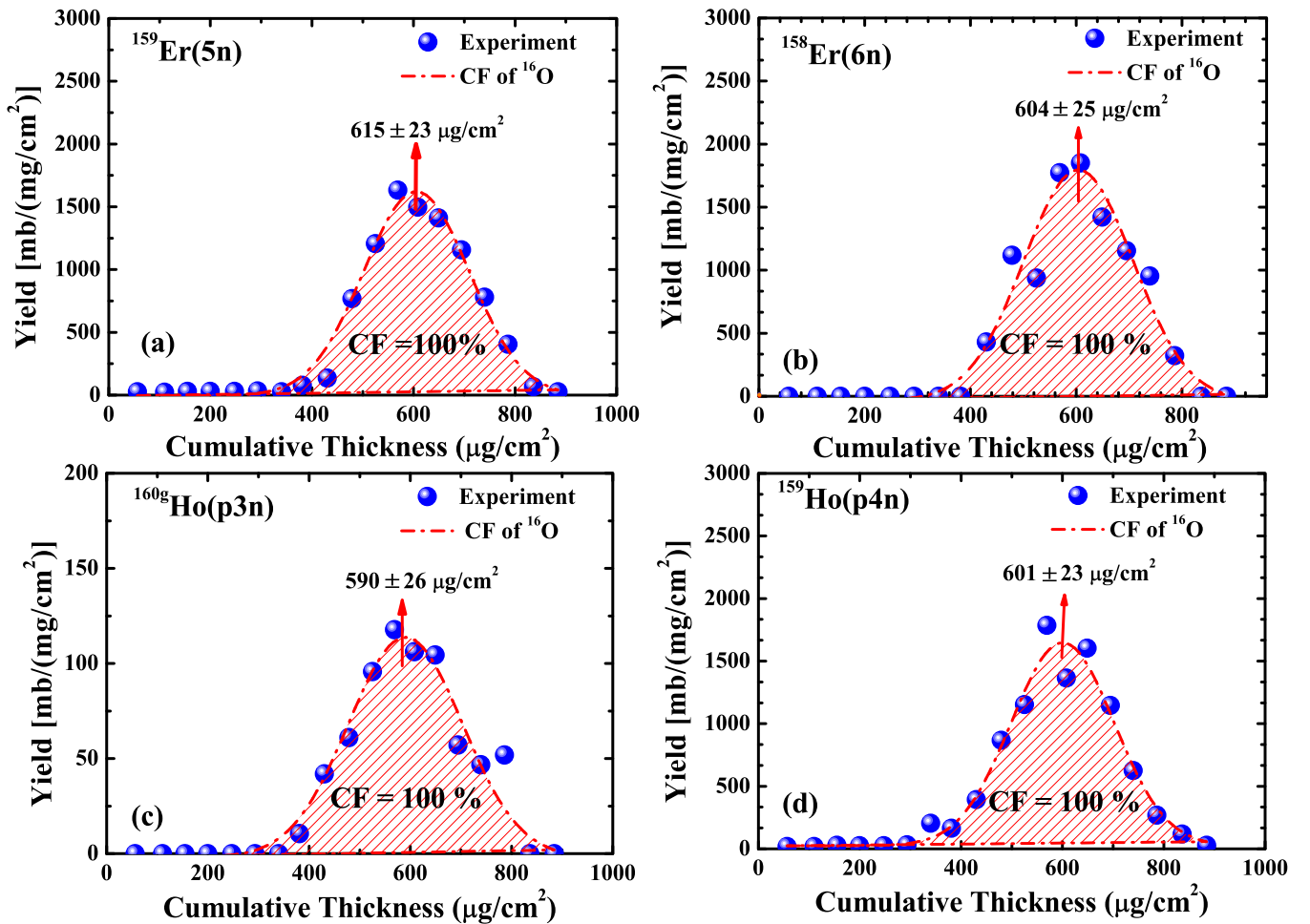

FIG. 4. Measured FRRDs for the ERs ^{159}Er(5n), ^{158}Er(6n), ^{160g}Ho(p3n), and ^{159}Ho(p4n) produced in ^{16}O + ^{148}Nd system at projectile energy ≈ 6 MeV/nucleon. Solid circles are the experimental data and dash-dotted curves represent the Gaussian fit to the measured FRRDs for CF of ^{16}O with ^{148}Nd.
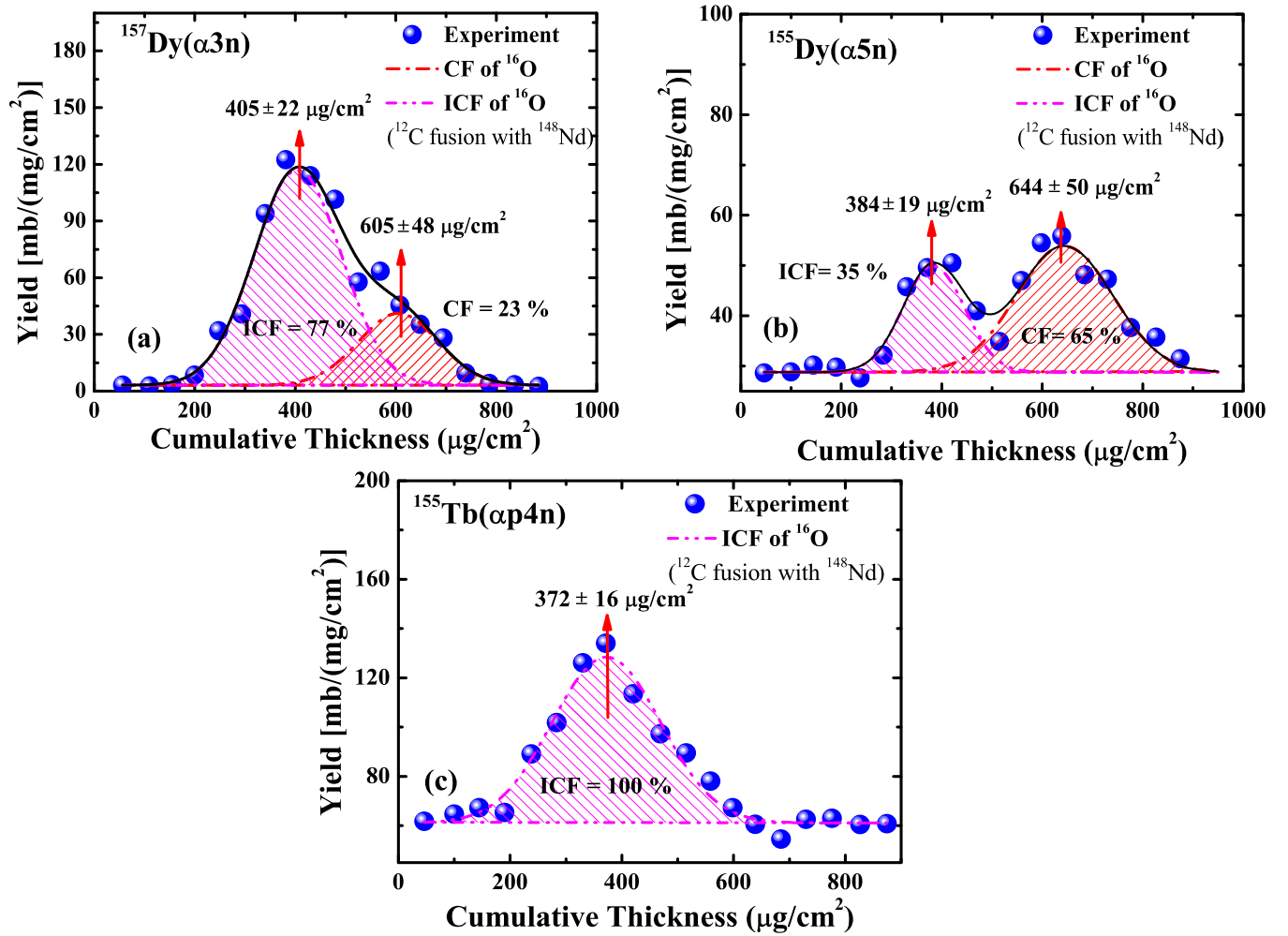
FIG. 5. Measured FRRDs for the ERs ^{157}Dy($\alpha 3n$), ^{155}Dy($\alpha 5n$), and ^{155}Tb($\alpha p4n$), respectively produced in ^{16}O + ^{148}Nd system at projectile energy $\approx$6 MeV/nucleon. Solid circles are the experimental data and dashed-dot curves represent the Gaussian fit to the measured FRRDs for CF of ^{16}O with ^{148}Nd, while dashed-dot-dot represent the Gaussian fit to the measured FRRDs ICF of ^{16}O (fusion of fragment ^{12}C).

The measured range integrated cross sections ($\sigma_{\text{Expt}}^{FRRD}$) of ERs produced via CF and ICF in the ^{16}O + ^{148}Nd system along with their theoretical cross sections of PACE4 ($\sigma_{\text{Theo}}^{PACE4}$) and CASCADE ($\sigma_{\text{Theo}}^{\text{CASCADE}}$) are given in Table III. It can be

TABLE III. Experimentally measured range integrated cross section deduced from FRRDs curves and theoretically calculated cross section by PACE4 code.

S. No.	Evaporation Residues	$\sigma_{\text{Expt}}^{FRRD}$ (mb)	$\sigma_{\text{Theo}}^{PACE4}$ (mb)	$\sigma_{\text{Theo}}^{\text{CASCADE}}$ (mb)
1.	^{159}Er(5n)	422.14	424.00	406.00
2.	^{158}Er(6n)	446.52	484.00	397.10
3.	^{160g}Ho($p3n$)	31.89[a]	20.90[a]	20.80[a]
4.	^{159}Ho($p4n$)	556.23[a]	475.80[a]	448.50[a]
5.	^{157}Dy($\alpha 3n$)	35.09	5.80	6.40
6.	^{155}Dy($\alpha 5n$)	32.87	17.10	21.50
7.	^{155}Tb($\alpha p4n$)	66.94[a]	17.36[a]	21.60[a]

[a]Cumulative cross section.

observed from this table that the ($\sigma_{\text{Expt}}^{FRRD}$) of ERs ^{159}Er(5$n$) and ^{158}Er(6$n$) satisfactorily reproduced with both PACE4 and CASCADE predictions. It is already mentioned that the ERs ^{160g}Ho($p3n$) and ^{159}Ho ($p4n$) may also populate through the EC/β^+ decay of their higher charge precursor isobars. Hence, the measured cumulative cross sections for these ERs were compared with the theoretical cumulative cross sections of PACE4 and CASCADE codes as given in Table III. The theoretical cumulative cross sections of PACE4 and CASCADE for an ER are the sum of theoretical predictions of its higher charge precursor isobars. In this table experimental and theoretical cumulative cross sections are marked by asterisk (*). As can be noticed from this table that the measured and theoretical cumulative cross sections of ERs ^{159,160}Ho (pxn) are in good agreement. This agreement shows that the ERs ^{159,160}Ho are predominantly populated via CF only. On the other hand, the measured cross sections of ERs ^{155}Dy and ^{157}Dy, populated via αxn emitting channels are found to be significantly enhanced over their theoretical predictions of PACE4 and CASCADE codes. This enhancement in measured
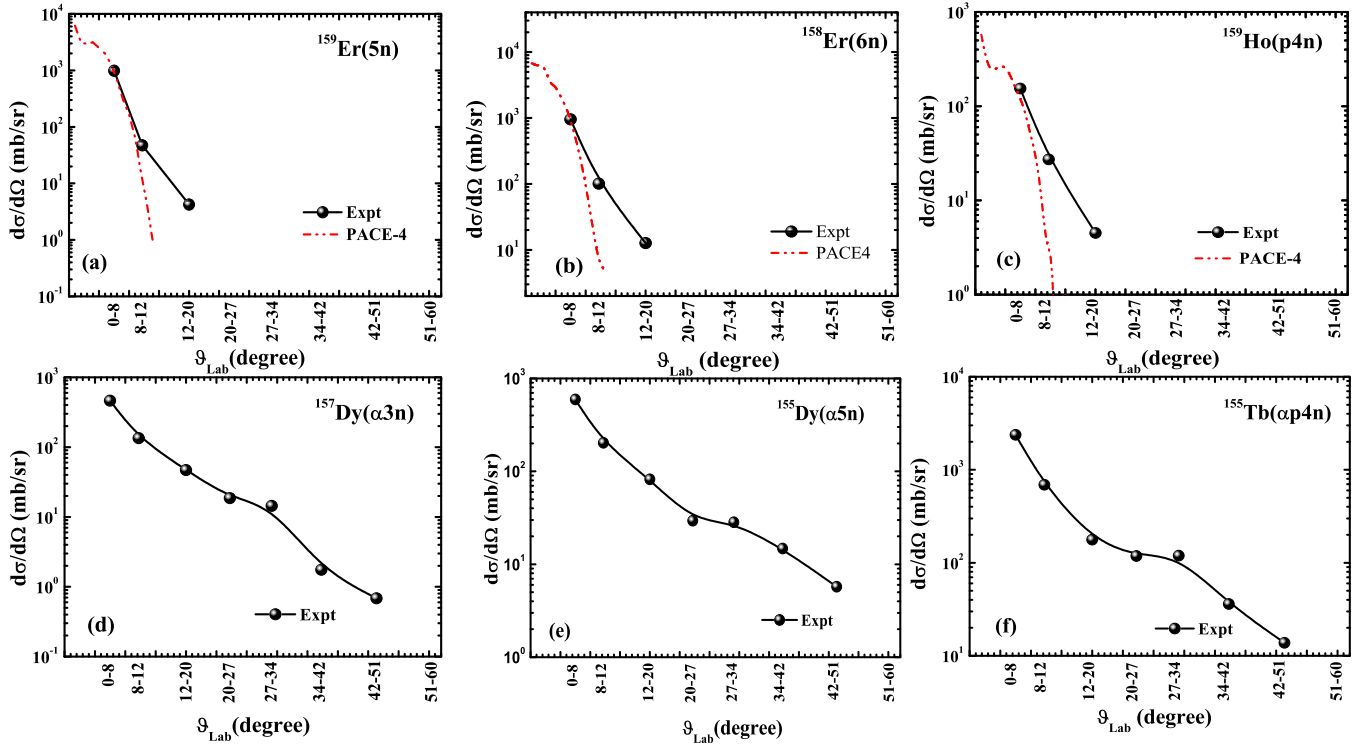
FIG. 6. Measured angular distributions for (a)-(c) ERs ^{159}Er($5n$), ^{158}Er($6n$), ^{159}Ho($p4n$) populated via complete fusion along with theoretical predictions of PACE4 code and (d)-(f) for ERs ^{157}Dy($\alpha 3n$), ^{155}Dy($\alpha 5n$), and ^{155}Tb($\alpha p4n$) populated via CF and/or ICF for the ^{16}O $+$ ^{148}Nd system at projectile energy ≈ 6 MeV/nucleon.

cross section is attributed to the break-up of ^{16}C into ^{12}C $+$ ^{4}He (α), whereas ^{12}C fuses with target ^{148}Nd and α behaves as a spectator (i.e., ICF of ^{16}O with ^{148}Nd). Furthermore, due to precursor isobar contribution in the production of ER ^{155}Tb($\alpha p4n$), the measured cumulative cross sections of this ER were compared with the theoretical cumulative cross sections of PACE4 and CASCADE in Table III. It can be seen clearly that the measured cumulative cross section for this ER is much enhanced over theoretical predictions. This means that the ER ^{155}Tb is mainly populated via ICF. These present results are supported by our earlier findings [25] through the measurements of excitation functions of the ERs populated via CF and ICF dynamics in the same projectile energy and system. As such, the above comparison of the measured FRRDs data with theoretical codes validates the consistency and reliability of the present results for ^{16}O $+$ ^{148}Nd system at projectile energy ≈ 6 MeV/nucleon.

B. Angular distributions (ADs) of ERs

An attempt was made to understand the heavy-ion reaction dynamics through ADs of ERs at projectile energy above the Coulomb barrier. The ADs of six ERs ^{159,158}Er(xn), ^{159}Ho(pxn), ^{157,155}Dy(αxn), and ^{155}Tb(αpxn) produced in the system ^{16}O $+$ ^{148}Nd were measured at projectile energy ≈ 6 MeV/nucleon. The measured cross section of each angular ring was divided by its corresponding solid angle to get the differential cross section of ERs. The differential cross sections plotted as a function of different angular zones are called ADs of ERs. The ADs of ERs may provide

significant information about the reaction dynamics involved in heavy-ion interactions. The theoretical ADs of ERs can be theoretically calculated using the statistical model code PACE4, which employs a Hauser-Feshbach formalism to describe the deexcitation of the fusion products. At this energy, the yields for all ERs were found to decrease with increase in laboratory angle. The PACE4 calculations for the present system show that the ERs are emitted within a folding angle of $\pm 14°$, peaking at around $5°$. The measured ADs of ERs ^{159}Er($5n$), ^{158}Er($6n$), and ^{159}Ho($p4n$) along with their theoretical predictions of PACE4 code were plotted in Figs. 6(a)–6(c). It can be seen from these figures that the ERs ^{159}Er, ^{158}Er, and ^{159}Ho were found to be emitted in smaller forward angles, peaking at around $0°$–$8°$ with respect to the beam direction. The measured ADs were satisfactorily reproduced by the PACE4 calculations for angular zone $0°$–$12°$. However, the measured values of ADs were found larger than PACE4 results for angles greater than $12°$ for these residues. This small discrepancy may be due to the limitations of theoretical code and experimental uncertainties. The measured ADs of ERs ^{157,155}Dy(αxn), and, ^{155}Tb(αpxn) were also plotted and shown in Figs. 6(d)–6(f). The theoretical ADs of PACE4 code for these ERs were found to have negligible values as compared to their measured ADs and hence, they are not displayed in Figs. 6(d)–6(f). As can be seen from these plots, the ERs ^{157,155}Dy, and ^{155}Tb are found to have contributions also at larger angles peaking in angular zones $0°$–$8°$ and $27°$–$34°$. From the present ADs results, it may be inferred that the ERs populated through xn/pxn channels are emitted up to angular zone $12°$–$20°$, while the ERs populated
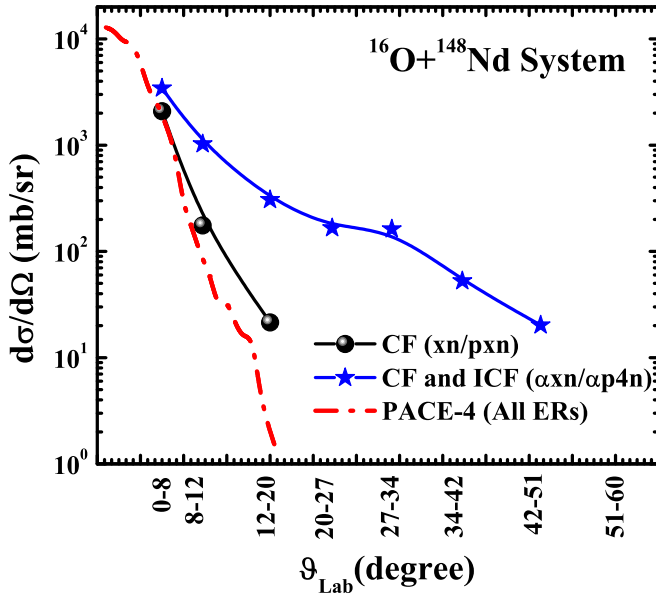
FIG. 7. Measured total fusion (CF + ICF) and CF ($xn + pxn$) angular distributions along with theoretical predictions of PACE4 code for the $^{16}O + ^{148}Nd$ system at projectile energy ≈6 MeV/nucleon.

through $\alpha xn/\alpha pxn$ channels are emitted in the larger angular zone up to 42°–51°. It was noticed from these figures that the angular distributions have two components, which are different in nature. This can be clearly understood as described below. The deexcitation of ER through single or few nucleon emission (xn/pxn channels) will transfer less momentum to the recoiling ER, which results in an angular distribution peaking at smaller angles. On the other hand, the emission of α particle ($\alpha xn/\alpha pxn$ channels) will impart larger momentum for the ER and hence produce an angular distribution peaking at larger angles. The component of the smaller angular zone of these distributions is satisfactorily described by the statistical model code. While, the theoretical code fails to predict the component of the larger angular zone. As such, the ADs for the ERs $^{157}Dy(\alpha 3n)$, $^{155}Dy(\alpha 5n)$, and $^{155}Tb(\alpha p4n)$ emitted in smaller angular zone 0°–20° may be assigned to the population of residues via CF whereas those emitted in the angular range ≈20°–51° may be attributed to the ICF processes. Further, the sum of measured differential cross sections for ICF (α-emitting) and CF (xn- and pxn-emitting) channels has been estimated and compared with the sum of theoretical differential cross sections for all ERs of PACE4 as a function of different angular zones as shown in Fig. 7. A reasonably good agreement between measured angular distribution for ERs produced via CF with PACE4 predictions was observed, while it did not match for ERs populated via ICF. In this figure, the dash-dotted curve represents the sum of theoretical differential cross sections of all ERs of PACE4 for the $^{16}O + ^{148}Nd$ at projectile energy ≈6 MeV/nucleon. The sum of measured differential cross sections of ERs ^{159}Er, ^{158}Er, and ^{159}Ho is shown by solid circles in this figure. This comparison clearly confirms the fact that the ERs of ICF channels were populated in the larger angular zone as compared to ERs of CF channels.

IV. CORRELATION OF ICF FRACTION WITH VARIOUS ENTRANCE CHANNEL PARAMETERS

It is now possible to correlate the ICF fraction of various systems with various entrance channel parameters due to the availability of more experimental data on ICF dynamics. In the present study, the incomplete fusion fraction (F_{ICF}) for the system $^{16}O + ^{148}Nd$ was estimated from the measured FRRDs data.

A new factor $L_R = (\ell_{max} - \ell_{crit})/\ell_{max}$ has been introduced in our earlier work [41] for normalization of experimental data to disentangle the entrance channel effects on ICF dynamics, where ℓ_{crit} and ℓ_{max} are the critical and maximum angular momenta limit of the system. These values have been calculated using formalism [14]. The angular momenta limit of CF and ICF channels were considered through this new parameter. Therefore this normalization factor is more suitable than other factors used in earlier measurements for comparison of experimental data of several projectile-target combinations. The ICF fraction from the measured FRRDs data was estimated for the present system $^{16}O + ^{148}Nd$ and compared with those obtained for $^{16}O + ^{148}Nd$ [25], ^{124}Sn [41], ^{103}Rh [42], ^{115}In [43], ^{93}Nb [44], ^{165}Ho [45], ^{51}V [46]; $^{20}Ne + ^{165}Ho$ [47], ^{59}Co [48], ^{55}Mn [49]; $^{13}C + ^{175}Lu$ [50], ^{169}Tm [51], ^{159}Tb [52], ^{165}Ho [53]; $^{12}C + ^{175}Lu$ [50], ^{159}Tb [54], ^{115}In [55] systems at a constant value of $L_R = (\ell_{max} - \ell_{crit})/\ell_{max} = 0.14$. In these measurements, some of the ERs could not be measured due to their very long or short half-lives, low branching ratio, and stability, etc. As such, the deduced F_{ICF} should be considered as lower limit of ICF contribution for the present system.

A. Dependence of ICF dynamics on entrance channel mass asymmetry, Coulomb factor, and α-Q value

Several studies [18–21] have shown that entrance channel mass asymmetry (μ_{EC}^{AS}), Coulomb factor ($Z_P Z_T$), and the α-Q value of projectile and the target deformation parameter (β_2^T) play an important role in ICF dynamics. An effort was made to investigate the dependence of ICF dynamics through the above-mentioned parameters at energy above the Coulomb barrier. As such, the deduced ICF fraction for the present and other systems taken from the literature [25,41–55] have been plotted as a function of mass asymmetry (μ_{EC}^{AS}) of interacting nuclei, Coulomb factor ($Z_P Z_T$), and α-Q value of projectile are displayed in Figs. 8(a)–8(c). As can be seen clearly from these plots that the ICF fraction rises exponentially with mass asymmetry (μ_{EC}^{AS}), Coulomb factor ($Z_P Z_T$), and α-Q value of projectile, independently for different projectiles. These present FRRDs results clearly show that the ICF dynamics is dependent on the mentioned parameters. However, the pattern of ICF fraction has been found exponential growth in above systematics, which is in contrast with the linear pattern as earlier measurements [18–21]. Moreover, the present systematic study also suggests that the ICF dynamics not only depend on the single entrance channel parameter but affected by all these parameters simultaneously. Here, it is also important to mention that the ICF fraction patterns with different entrance channel parameters are strongly dependent on incident projectile energy and the choice of normalization factor.
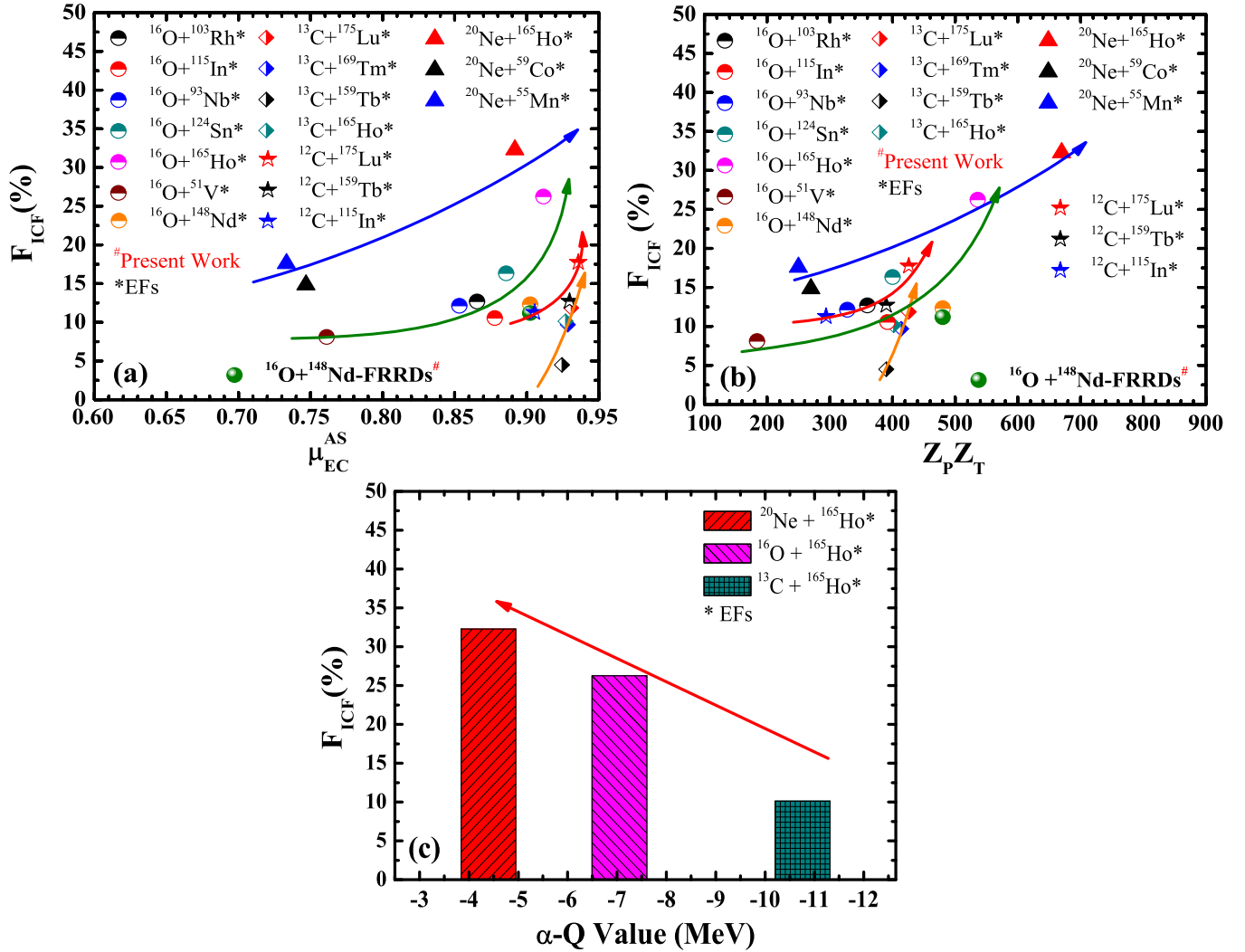
FIG. 8. The incomplete fusion fraction (F_{ICF}) for the present system $^{16}O + ^{148}Nd$ along with other systems [25,41–55] as a function of (a) μ_{EC}^{AS}, (b) $Z_P Z_T$, and (c) α-Q value at a constant value $(\ell_{max} - \ell_{crit})/\ell_{max} = 0.14$. The solid lines are drawn to represent the incomplete fusion fraction (F_{ICF}) data for different projectiles.

B. Dependence of ICF dynamics on target deformation

Some recent studies suggested that the ICF dynamics depends on the deformation of the target (β_2^T) [23–25]. Further, no systematic pattern of ICF fraction has been found by the investigation [19] using this parameter. As such, the correlation of ICF dynamics with the structure of the target is still a dilemma. However, to reach on a definite conclusion about the dependence of ICF dynamics on β_2^T, more investigation is required. In this respect, a systematics about the deformation and structure of the target has been presented in this section. The deduced values of F_{ICF} for the present system along with other systems taken from literature [25,41–55] were plotted as a function of β_2^T and displayed in Fig. 9(a). As can be seen from this figure that the ICF fraction rises almost exponentially with β_2^T, but the rising rates are different for different projectiles. The different rising rates of ICF fraction indicate that the ICF dynamics not only depends on the deformation of the target nuclei, but it also depends on the projectile

structure. The values of β_2^T for different targets were taken from Ref. [56].

Further, the effect of different size of interacting partners was investigated through the interaction radius of target (R^T). The interaction radius is a well-known parameter to determine the size of spherical nuclei and directly related to the mass number of nuclei. The values of R^T were calculated using the formulation in Ref. [57]. To observe the effect of R^T on ICF dynamics, the ICF fraction was plotted as a function of interaction radius of target (R^T) and displayed in Fig. 9(b). From Fig. 9(b), it can be observed that the ICF fraction grows exponentially with R^T for systems having same projectile. However, it was also noticed that the data points of F_{ICF} are more spread out than the exponential rise pattern (systematics) observed in Fig. 9(a). This discrepancy is more clearly observed in case of ^{16}O projectile systems. This discrepancy may be due to noninclusion of deformation effects in the parameter R^T. These present observations suggest that the interaction radius (R^T) is not a suitable parameter to encounter
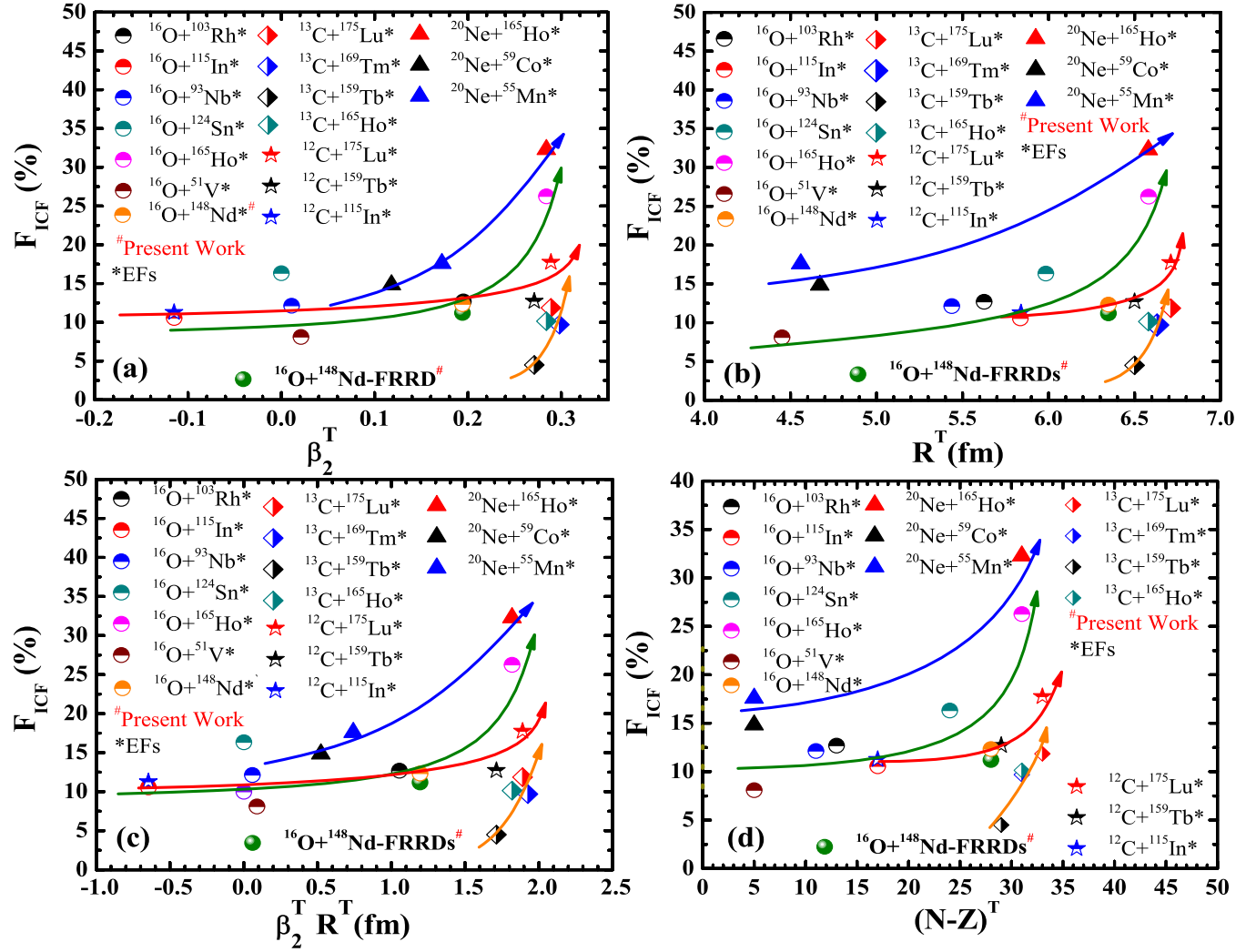
FIG. 9. The incomplete fusion fraction (F_{ICF}) for the present system $^{16}O + ^{148}Nd$ along with other systems [25,41–55] as a function of (a)β_2^T, (b) R^T, (c) $\beta_2^T R^T$, and (d) $(N-Z)^T$ at a constant value $(\ell_{max} - \ell_{crit})/\ell_{max} = 0.14$. The solid lines are drawn to represent the incomplete fusion fraction (F_{ICF}) data for different projectiles.

the deformation effects in the study of low-energy ICF dynamics. However, this parameter can be used to explain the ICF characteristics only for the interaction of spherical projectile and target (i.e., spherical-spherical interactions). The ICF dynamics is also expected to be influenced by the relative orientations (i.e., tip-tip or side-side) of the interacting partners along with their shapes. The different relative orientations give rise to different angular momenta and nuclear overlap in the collision of deformed projectile and target. Hence, the effect of orientation of nuclei should be considered along with their deformation (oblate or prolate). Consequently, the effects of different shapes of interacting partners along with their relative orientations on ICF dynamics were also studied through the target deformation length ($\beta_2^T R^T$). The target deformation length ($\beta_2^T R^T$) is the multiplication of the target deformation parameter (β_2^T) with interaction radius of the target (R^T). The interaction of a system depends on the deformation (oblate or prolate) and orientation of interacting partners. Thus, the total and ICF cross sections are also dependent on the shape and orientation of the nuclei. The target

deformation length ($\beta_2^T R^T$) is able to explain the effects of both shape and orientation of colliding nuclei simultaneously. In this respect, the deduced values of F_{ICF} for the present system along with literature data [25,41–55] have been plotted as a function of $\beta_2^T R^T$ and shown in Fig. 9(c). This plot clearly shows that the ICF fraction rises exponentially with $\beta_2^T R^T$, independently for different projectiles. It means that the probability of ICF increases with $\beta_2^T R^T$, while the rising rate of ICF contribution depends on the deformation and relative orientations of colliding partners. It is important to mention that the spread out of data points observed in case of R^T is washed out in the systematics of $\beta_2^T R^T$. This may be due to the inclusion of deformation effect of target in $\beta_2^T R^T$. These present results show that the parameter $\beta_2^T R^T$ is more suitable than simply R^T to explain the dependence of ICF dynamics on the deformation and orientations of interacting nuclei. The present analysis shows that the ICF dynamics is significantly affected by the shapes and relative orientations of colliding partners simultaneously. These effects are clearly observed with deformation length ($\beta_2^T R^T$). In addition, the

above-mentioned results obtained from β_2^T, R^T, and $\beta_2^T R^T$ systematics were further confirmed through another parameter excess of neutrons $(N - Z)^T$ in target, which is also associated with the target structure. The ICF fraction for the present system along with literature data [25,41–55] was plotted as a function of $(N - Z)^T$ and displayed in Fig. 9(d). As can be seen clearly in this figure, the ICF fraction rises exponentially also with $(N - Z)^T$, independently for different projectiles. Thus, the effect of structure the of target has been shown by four different parameters viz. β_2^T, R^T, $\beta_2^T R^T$, and $(N - Z)^T$. This study highlights the role of target structure on ICF dynamics. These present results are in contrast with the study on target deformation by Kumar *et al.* [19] at low projectile energy. It has been found from the present FRRDs analysis that these three parameters namely; β_2^T, $\beta_2^T R^T$, and $(N - Z)^T$ are required to investigate the role of the projectile and target deformation on ICF dynamics. These three parameters are associated with the structure of the colliding nuclei and interaction process. Hence, these parameters should also be considered as important tools to probe the effects of the projectile and target deformation on ICF dynamics at low projectile energy. The systematic review on the existing entrance channel effects along with some new parameters indicates that the ICF dynamics is strongly influenced by the structure of both projectile and the target. Earlier studies available in the literature [18–21] have observed a simple linear pattern of ICF fraction with various entrance channel parameters. However, the present results clearly show that the ICF fraction rises exponentially with entrance channel parameters in contrast to a simple linear growth.

V. SUMMARY AND CONCLUSIONS

The study of incomplete fusion dynamics was done by the measurements of forward recoil range distributions (FRRDs) and angular distributions (ADs) of evaporation residues (ERs) populated in the $^{16}O + ^{148}Nd$ system at same projectile energy ≈ 6 MeV/nucleon. Different linear momentum transfer components were observed in FRRDs measurements, which may be attributed to the break-up of ^{16}O projectile into ^{12}C and α particle. The analysis of FRRDs indicates a significant contribution from the partial linear momentum transfer (LMT) of the projectile associated with incomplete fusion (ICF) in the production of residues populated via several α-emitting channels. The relative contributions of complete fusion (CF) and/or ICF components were extracted from the FRRDs data. The results of FRRDs were also confirmed by the measurements of ADs of ERs at same projectile energy. The present results of ADs reveal that the ERs populated via xn/pxn channels are emitted in the angular zone $\approx 0°$-$20°$. These results were found to be in good agreement with the theoretical predictions made by PACE4 code for ADs. It means

that these ERs are expected to be populate through only CF of ^{16}O with ^{148}Nd. However, the ERs populated via $\alpha xn/\alpha pxn$ channels were found to be trapped at larger angular zone $\approx 0°$-$51°$ as compared to PACE4 predictions for CF channels. These ADs results show that the ERs populated through α-emission channels have contribution from ICF in addition to CF. Further, a systematic study was done to correlate the ICF fraction with various entrance channel parameters. This systematic study on well-known entrance channel parameters suggests that the ICF fraction increases exponentially with mass asymmetry (μ_{EC}^{AS}) between interacting partners, Coulomb factor ($Z_P Z_T$), and α-Q value of projectile. Further, the effect of the structure of target on ICF dynamics was investigated through four different parameters viz. deformation of target (β_2^T), interaction radius of target (R^T), target deformation length ($\beta_2^T R^T$), and neutron excess $(N - Z)^T$ of the target. In the present study, the ICF contribution was found to increase exponentially with the parameters β_2^T, R^T, $\beta_2^T R^T$, and $(N - Z)^T$, independently for individual projectiles. These parameters were found very sensitive and useful to probe the role of the deformation of the projectile and the target along with their structures. The present analysis also suggests that the parameter $\beta_2^T R^T$ is more effective than R^T to encounter the dependence of ICF dynamics on the deformation and relative orientations of interacting partners. However, the parameter R^T can be used to explain the behavior of ICF dynamics only for the collision of spherical-spherical nuclei. Finally, these present results clearly indicate that the ICF fraction follows exponential pattern rather than a simple linear growth with entrance channel parameters as suggested by earlier works. This systematic pattern indicates that the ICF dynamics is strongly influenced by the structure of projectile along with the target.

[1] P. E. Hodgson, *Nuclear Heavy Ion Reactions* (Clarendon Press, Oxford, 1978).

[2] D. J. Parker, J. J. Hogan, and J. Asher, Phys. Rev. C **35**, 161 (1987).

[3] B. S. Tomar, A. Goswami, A. V. R. Reddy, S. K. Das, P. P. Burte, S. B. Manohar, and B. John, Phys. Rev. C **49**, 941 (1994).

[4] S. Chakrabarty, B. S. Tomar, A. Goswami, G. K. Gubbi, S. B. Manohar, A. Sharma, B. B. Kumar, and S. Mukherjee, Nucl. Phys. A **678**, 355 (2000).

[5] P. E. Hodgson and E. Gadioli, *Introductory Nuclear Physics* (Oxford University Press, Oxford, 1997).

[6] H. C. Britt and A. R. Quinton, Phys. Rev. **124**, 877 (1961).

[7] T. Inamura, M. Ishihara, T. Fukuda, T. Shimoda, and H. Hiruta, Phys. Lett. B **68**, 51 (1977).

[8] D. J. Parker, J. Asher, T. W. Conlon, and I. Naqib, Phys. Rev. C **30**, 143 (1984).

[9] I. Tserruya, V. Steiner, Z. Fraenkel, P. Jacobs, D. G. Kovar, W. Henning, M. F. Vineyard, and B. G. Glagola, Phys. Rev. Lett. **60**, 14 (1988).

[10] M. Crippa, E. Gadioli, G. Ciavola, C. Marchetta, and M. Bonardi, Z. Phys. A **350**, 121 (1994).

[11] B. S. Tomar, A. Goswami, G. K. Gubbi, A. V. R. Reddy, S. B. Manohar, B. John, and S. K. Kataria, Phys. Rev. C **58**, 3478 (1998).

[12] D. Singh, M. A. Ansari, R. Ali, N. P. M. Sathik, B. S. Tomar, and M. Ismail, J. Phys. Soc. Jpn. **82**, 114201 (2013).

[13] T. Udagawa and T. Tamura, Phys. Rev. Lett. **45**, 1311 (1980).

[14] J. Wilczynski, K. Siwek-Wilczynska, J. Van Driel, S. Gonggrijp, D. C. J. M. Hageman, R. V. F. Janssens, J. Lukasiak, R. H. Siemssen, and S. Y. Van der Werf, Nucl. Phys. A **373**, 109 (1982).

[15] J. P. Bondrof, J. N. De, G. Fai, A. O. T. Karvinen, B. Jakobsson, and J. Randrup, Nucl. Phys. A **333**, 285 (1980).

[16] M. I. Sobel, P. J. Siemens, J. P. Bondrof, and H. A. Bethe, Nucl. Phys. A **251**, 502 (1975).

[17] D. H. E. Gross and J. Wilczynski, Phys. Lett. B **67**, 1 (1977).

[18] H. Morgenstern, W. Bohne, W. Galster, and K. Grabisch, Z. Phys. A **324**, 443 (1986).

[19] H. Kumar, S. A. Tali, M. Afzal Ansari, D. Singh, R. Ali, K. Kumar, N. P. M. Sathik, A. Ali, S. Parashari, R. Dubey, I. Bala, R. Kumar, R. P. Singh, and S. Muralithar, Eur. Phys. J. A **54**, 47 (2018).

[20] A. Yadav, P. P. Singh, M. Shuaib, V. R. Sharma, I. Bala, Unnati, S. Gupta, D. P. Singh, M. K. Sharma, R. Kumar, S. Murlithar, R. P. Singh, B. P. Singh, and R. Prasad, Phys. Rev. C **96**, 044614 (2017).

[21] S. A. Tali, H. Kumar, M. A. Ansari, A. Ali, D. Singh, R. Ali, P. K. Giri, S. B. Linda, R. Kumar, S. Parashari, S. Muralithar, and R. P. Singh, Phys. Rev. C **100**, 024622 (2019).

[22] R. Ali, M. A. Ansari, D. Singh, R. Kumar, D. P. Singh, M. K. Sharma, Unnati Gupta, B. P. Singh, P. D. Shidling, D. Negi, S. Muralithar, R. P. Singh, and R. K. Bhowmik, Nucl. Phys. A **968**, 403 (2017).

[23] D. Singh, S. B. Linda, P. K. Giri, A. Mahato, R. Tripathi, H. Kumar, M. A. Ansari, N. P. M. Sathik, R. Ali, R. Kumar, S. Muralithar, and R. P. Singh, Phys. Rev. C **97**, 064604 (2018).

[24] D. Singh, S. B. Linda, P. K. Giri, A. Mahato, R. Tripathi, H. Kumar, M. A. Ansari, N. P. M. Sathik, R. Ali, R. Kumar, S. Muralithar, and R. P. Singh, Phys. Lett. B **774**, 7 (2017).

[25] P. K. Giri, D. Singh, A. Mahato, S. B. Linda, H. Kumar, S. A. Tali, S. Parasari, A. Ali, M. A. Ansari, R. Dubey, R. Kumar, S. Muralithar, and R. P. Singh, Phys. Rev. C **100**, 024621 (2019).

[26] M. Thakur, R. Dubey, S. R. Abhilash, B. R. Behera, B. P. Mohanty, D. Kabiraj, S. Ojha, and H. Duggal, MethodsX **3**, 542 (2016).

[27] N. K. Deb, K. Kalita, S. R. Abhilash, P. K. Giri, R. Biswas, G. R. Umapathy, D. Kabiraj, and S. Chopra, Vacuum **163**, 148 (2019).

[28] B. P. A. Kumar, E. T. Subramaniam, K. Singh, R. K. Bhowmik, DAE-BRNS Nucl. Phys. Symp., Kolkata, 2001 (unpublished), http://www.iuac.res.in/NIAS/

[29] S. Y. F. Chu, L. P. Ekstrom, and R. B. Firestone, The Lund/LBNL Nuclear Data Search, Version 2.0, 1999, http://nucleardata.nuclear.lu.se/toi/index.asp

[30] National Nuclear Data Centre, Brookhaven National Laboratory, https://www.nndc.bnl.gov/nudat2/

[31] J. K. Tuli, *Nuclear Wallet Cards*, 8th ed., (National Nuclear Data Centre, Upton, 2011).

[32] M. A. Ansari, R. K. Y. Singh, M. L. Sehgel, V. K. Mittal, D. K. Avasthi, and I. M. Govil, Ann. Nucl. Energy **11**, 607 (1984).

[33] ORIGIN (Origin Lab, Northampton, Massachusetts); http://www.originlab.com/

[34] D. Singh, R. Ali, M. A. Ansari, M. H. Rashid, R. Guin, and S. K. Das, Phys. Rev. C **79**, 054601 (2009).

[35] The Stopping and Range of Ions in Matter (SRIM-2008.04); http://www.srim.org/

[36] A. Gavron, Phys. Rev. C **21**, 230 (1980).

[37] O. B. Tarasov and D. Bazin, NIM B **266**, 4657 (2018).

[38] http://lise.nscl.msu.edu/pace4

[39] F. Puhlhofer, Nucl. Phys. A **280**, 267 (1977).

[40] W. Hauser and H. Feshbach, Phys. Rev. **87**, 366 (1952).

[41] D. Singh, S. B. Linda, P. K. Giri, A. Mahato, R. Tripathi, H. Kumar, S. A. Tali, S. Parashari, A. Ali, R. Dubey, M. A. Ansari, R. Kumar, S. Muralithar, and R. P. Singh, Phys. Rev. C **97**, 064610 (2018).

[42] U. Gupta, P. P. Singh, D. P. Singh, M. K. Sharma, A. Yadav, R. Kumar, B. P. Singh, and R. Prasad, Nucl. Phys. A **811**, 77 (2008).

[43] K. Kumar, T. Ahmad, S. Ali, I. A. Rizvi, A. Agarwal, R. Kumar, and A. K. Chaubey, Phys. Rev. C **88**, 064613 (2013).

[44] A. Sharma, B. B. Kumar, S. Mukherjee, S. Chakrabarty, B. S. Tomar, A. Goswami, and S. B. Manohar, J. Phys. G: Nucl. Part. Phys. **25**, 2289 (1999).

[45] K. Kumar, T. Ahmad, S. Ali, I. A. Rizvi, A. Agarwal, R. Kumar, K. S. Golda, and A. K. Chaubey, Phys. Rev. C **87**, 044608 (2013).

[46] S. Mukherjee, A. Sharma, S. Sodaye, B. S. Tomar, A. Goswami, and S. B. Manohar, Eur. Phys. J. A **12**, 199 (2001).

[47] D. Singh, Rahbar Ali, M. Afzal Ansari, M. H. Rashid, R. Guin, and S. K. Das, Nucl. Phys. A **879**, 107 (2012).

[48] D. Singh, R. Ali, M. Afzal Ansari, B. S. Tomar, M. H. Rashid, R. Guin, and S. K. Das, Phys. Rev. C **83**, 054604 (2011).

[49] Rahbar Ali, D. Singh, M. Afzal Ansari, M. H. Rashid, R. Guin, and S. K. Das, J. Phys. G: Nucl. Part. Phys. **37**, 115101 (2010).

[50] H. Kumar, S. A. Tali, M. A. Ansari, D. Singh, R. Ali, K. Kumar, N. P. M. Sathik, S. Parashari, A. Ali, R. Dubey, I. Bala, R. Kumar, R. P. Singh, and S. Muralithar, Nucl. Phys. A **960**, 53 (2017).

[51] V. R. Sharma, A. Yadav, P. P. Singh, D. P. Singh, S. Gupta, M. K. Sharma, I. Bala, R. Kumar, S. Murlithar, B. P. Singh, and R. Prasad, Phys. Rev. C **89**, 024608 (2014).

[52] A. Yadav, V. R. Sharma, P. P. Singh, R. Kumar, D. P. Singh, Unnati, M. K. Sharma, B. P. Singh, and R. Prasad, Phys. Rev. C **86**, 014603 (2012).

[53] S. A. Tali, H. Kumar, M. A. Ansari, A. Ali, D. Singh, R. Ali, P. K. Giri, S. B. Linda, S. Parashari, R. Kumar, R. P. Singh, and S. Muralithar, Nucl. Phys. A **970**, 208 (2018).

[54] A. Yadav, V. R. Sharma, P. P. Singh, D. P. Singh, M. K. Sharma, U. Gupta, R. Kumar, B. P. Singh, R. Prasad, and R. K. Bhowmik, Phys. Rev. C **85**, 034614 (2012).

[55] S. Mukherjee, A. Sharma, S. Sodaye, A. Goswami, and B. S. Tomar, Int. J. Mod. Phys. E **15**, 237 (2006).

[56] P. Moller, A. Sierk, T. Ichikawa, and H. Sagawa, At. Data Nucl. Data Tables **109–110**, 1 (2016).

[57] W. Wilcke, J. Birkelund, H. Wollersheim, A. Hoover, J. Huizenga, W. Schroder, and L. Tubbs, At. Data Nucl. Data Tables **25**, 389 (1980).